Magnetoelectric vertically aligned nanocomposite of YFeO₃ and

CoFe₂O₄

Abinash Kumar[†], Shuai Ning^{†*}, Tingyu Su, Eunsoo Cho, James M. LeBeau and Caroline A. Ross^{*}

A. Kumar, T. Su, E. Cho, J. M. LeBeau, C. A. Ross

Department of Materials Science and Engineering, Massachusetts Institute of Technology,

Cambridge, Massachusetts 02139, USA

E-mail: <u>caross@mit.edu</u> (C.A.R.)

S. Ning

School of Materials Science and Engineering, Nankai University, Tianjin 300350, P. R. China.

E-mail: sning@nankai.edu.cn (S.N.)

Keywords: vertically aligned nanocomposite, YFeO₃, CoFe₂O₄, magnetoelectric coupling,

Abstract

Self-assembled two-phase vertically aligned nanocomposites consisting of ferromagnetic pillars

embedded in a ferroelectric matrix provide an attractive geometry for observing magnetoelectric

coupling based on the strain-coupled magnetostrictive and piezoelectric effects at the interfaces.

In perovskite-spinel nanocomposites the ferroelectric phase typically consists of BiFeO₃, BaTiO₃

or Pb(Zr,Ti)O₃. Here, the ferroelectric phase is Y-rich YFeO₃ which exhibits ferroelectricity

originating from the local inversion symmetry breaking caused by Y_{Fe} antisite defects. Coherent

interfaces observed between Y-rich YFeO₃ and a magnetic spinel CoFe₂O₄ in a vertically aligned

nanocomposite enable strain-mediated magnetoelectric coupling at room temperature, confirming

the ferroelectricity and piezoelectricity in Y-rich YFeO3 and extending the range of

magnetoelectric nanocomposite compositions.

1

1. Introduction

Multiferroic materials, especially magnetoelectrics with coupled ferroelectric and magnetic behavior, have been studied extensively both for their interesting properties and for applications in memory or logic devices^[1]. Obtaining coexisting ferroelectricity and ferro- or ferrimagnetism in a single-phase material such as a perovskite-type (ABO₃) transition metal oxide is challenging^[2]. Considering the scarcity of single-phase multiferroics, an alternative strategy to realize magnetoelectric (ME) coupling is the integration of ferroelectric and magnetic materials into heterostructures or composites^[3-4], which rely on mechanical coupling between the magnetoelastic strain of the magnetic phase and the piezoelectric strain of the ferroelectric phase^[5-7].

According to the geometry or connectivity of each phase, ME composites can be classified into three categories: 0-3 type (particles buried in a matrix), 2-2 type (bilayer or multilayer films), and 1-3 type (rods or pillars embedded in a matrix). The 1-3 type nanocomposites are usually obtained by self-assembly of two immiscible phases on appropriate substrates to form vertical pillars in a matrix, as first demonstrated in epitaxial (La_{0.7}Ca_{0.3}MnO₃)_{1-x}:(MgO)_x films^[8]. The high density of vertical interfaces between the two phases of the 1-3 type nanocomposite make this system well suited for ME coupling because the clamping effect from substrate is orthogonal to the interfaces which enables a more efficient strain transfer between the phases.

Early work on 1-3 type ME nanocomposites reported magnetic CoFe₂O₄ (CFO) spinel pillars embedded in a ferroelectric BaTiO₃ (BTO) perovskite matrix^[9]. Since then, extensive research has explored the strain-mediated ME coupling mechanism, properties and applications of nanocomposites^[10-16]. However, the ferroelectric phase utilized in self-assembled ME nanocomposites has been selected from only a handful of well-known materials including BTO, BiFeO₃ (BFO) and Pb(Zr,Ti)O₃ (PZT)^[17]. Multiple unconventional mechanisms for improper

ferroelectrics have been discovered including geometrically^[18-21], electronically^[22-23], and magnetically ^[24] induced ferroelectricity and defect-mediated ferroelectricity^[25-28]. In particular, we recently showed that YFeO₃ (YFO) can be rendered ferroelectric by Y_{Fe} antisite defects that promote a local inversion symmetry breaking^[28].

Here, we report the synthesis and ME coupling of self-assembled nanocomposites consisting of CFO pillars in a ferroelectric Y-rich YFO matrix. Bulk YFO exhibits an orthorhombic perovskite structure with lattice parameters of a_0 =5.282 Å, b_0 =5.595 Å, c_0 =7.605 Å, or $a_p = \frac{1}{2} \sqrt{a_0^2 + b_0^2} = 3.847 \text{ Å}, c_p = c_0/2 = 3.803 \text{ Å}$ where subscripts o and p denote the orthorhombic cell and pseudocubic perovskite cell notation, respectively. CFO forms a cubic spinel structure with lattice parameter of $a_{p,CFO} = a_{CFO}/2 = 4.196$ Å. The epitaxial arrangement of YFO and CFO on the NSTO substrate is shown in Figure 1a, where lattice mismatch with the substrate is expected to cause in-plane tensile strain in the YFO and compressive strain in the CFO. Atomic resolution scanning transmission electron microscopy (STEM) reveals the phase separation and coherent interfaces between perovskite-structured YFO and spinel-structured CFO. As found in monolithic Y-rich YFO thin films^[28], Y_{Fe} antisite defects are present in the YFO matrix, enabling robust ferroelectric behavior of the nanocomposite. Strain-mediated ME coupling effect is observed upon applying an external magnetic field during piezoresponse force microscopy (PFM) measurements, not only corroborating the Y_{Fe} antisite-induced ferroelectricity and piezoelectricity in YFO but also extending the range of functional nanocomposites that exhibit ME coupling effects.

2. Results and Discussion

YFO-CFO nanocomposite thin films with thickness of 75 nm were deposited on (001)-oriented Nb-doped SrTiO₃ (NSTO) (cubic, a=3.905 Å) single crystal substrates by pulsed laser deposition (PLD) from YFO and CFO targets in oxygen atmosphere as described in the Experimental Section.

The ratio of laser shots ($n_{\rm YFO}/n_{\rm CFO}$) in each cycle of ablation of the YFO and CFO targets not only determines the volume fraction of each component but also affects the epitaxial quality of asgrown films. For $n_{\rm YFO}/n_{\rm CFO}$ =200:50, only (00l) peaks from the NSTO substrate, perovskite YFO and spinel CFO phases are seen in the 2θ - ω high-resolution X-ray diffraction (HRXRD) pattern (Figure 1b). For $n_{\rm YFO}/n_{\rm CFO}$ =100:100, the YFO maintains its (00l) orientation but the CFO volume fraction is higher and it exhibits polycrystalline growth with (lll) and (ll0) as well as (00l) peaks (data is not shown).

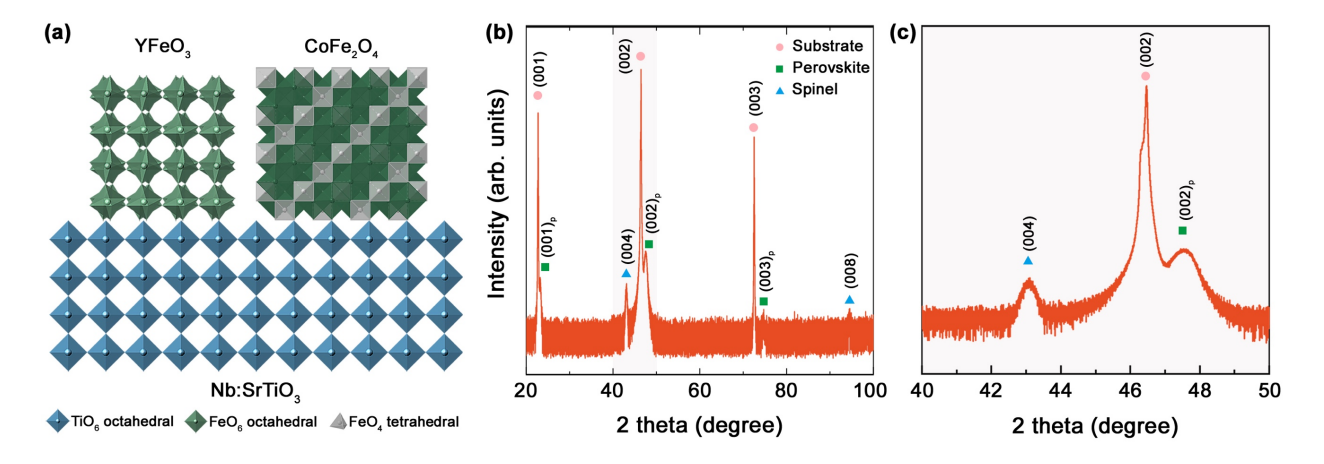


Figure 1. (a) Polyhedral model of YFO, CFO and NSTO crystal structures. (b) 2θ - ω full scan of YFO-CFO nanocomposite thin films grown on 001-oriented NSTO substrate with $n_{\rm YFO}/n_{\rm CFO}$ =200:50. (c) 2θ - ω HRXRD scan around the 002 peak of substrate.

The out-of-plane lattice parameters of YFO and CFO extracted from the 2θ - ω HRXRD scan around the (002) peak of the substrate (Figure 1c) are 3.820 Å and 2×4.199 Å, respectively. For the Y-rich YFO, an increase in unit cell volume compared to bulk stoichiometric YFO is expected due to the larger ionic radius of Y vs. Fe, but it is notable that the out-of-plane lattice parameter of the YFO matrix is also slightly larger than that of a single-phase YFO thin film (3.813 Å^[28]) grown

under the same conditions. For the CFO the out-of-plane lattice parameter is similar to the bulk value.

Cross-sectional high-angle annular dark-field (HAADF) STEM imaging and energy-dispersive X-ray spectroscopy (EDS) were performed to further analyze the microstructures of the YFO-CFO nanocomposite thin film. As shown in Figure 2a, phase separation is corroborated by the alternating Y-rich and Co-rich regions. Coherent interfaces are seen between YFO and CFO (Figure 2b). At the early stage of growth, the coherent interface between YFO and CFO (Figure 2d) forms an angle of ~53° with respect to the NSTO substrate surface, characteristic of (111)-type facets, the lowest specific surface energy planes, and similar to observations in BFO-CFO nanocomposites^[29]. As the nanocomposite grows thicker, the diameter of CFO pillars fluctuates by a few percent, and interfacial steps appear after ~12 nm thickness, Figure 2c, which help to accommodate large difference in lattice parameter between bulk YFO and CFO along growth direction. The mismatch is ~10% both in-plane and out-of-plane, evident from Fourier filtered images (Figure 2e&f) of the YFO-CFO interface. The orientation relationship between the two phases is (110)[001]_{YFO} // (110)[001]_{CFO} (Figure 2c&d), similar to that of BTO-CFO^[9] and BFO-CFO^[9] nanocomposites grown on (001)-oriented STO substrates.

Table 1. Strains of YFO and CFO in the nanocomposite analyzed from STEM at the bottom (substrate interface) and top of the film

	In-plane strain (%)		Out-of-plane strain (%)	
	Bottom	Тор	Bottom	Тор
YFO	-2.0	-2.7	+0.15	+0.40
CFO	-1.2	0.50	+1.0	+0.30

The lattice parameters and strains were also analyzed from the STEM data both near the substrate and near the top surface of the nanocomposite (see Table 1). Near the interface, the YFO is compressed in-plane by -2% (with a pseudocubic lattice parameter $a_{\rm p,\,bot}$ =3.77 Å) and expanded out-of-plane by +0.15% ($c_{\rm p,\,bot}$ =3.81 Å), whereas near the top of the nanocomposite it further contracts in-plane (to -2.7%, i.e., $a_{\rm p,\,top}$ =3.74 Å) and elongates out-of-plane (to +0.40%, $c_{\rm p,\,top}$ =3.82 Å). The out-of-plane values are close to that derived from XRD (3.820 Å) and that of monolithic thin film (3.813 Å)^[28], but the in-plane values are smaller than that of the single-phase film (3.862 Å)^[28] and of the substrate (3.905 Å). The YFO in the nanocomposite therefore exhibits an out-of-plane tensile strain which contrasts with the monolithic YFO film, which was under in-plane tensile strain. This suggests that the strain state of the YFO in the nanocomposite is dominated by the tensile strain imposed by the CFO at the vertical interfaces, whereas the strain in the single-phase film is dominated by the tensile strain imposed by the substrate.

For the CFO at the bottom region near to the substrate, it is compressed in-plane by -1.2% and expanded by 1% out-of-plane compared to its bulk value. The in-plane compression near the substrate is presumably caused by the epitaxial growth on the substrate, but the strain relaxes as the pillars grow taller, resulting in a slight in-plane expansion (+0.50%), as well as a suppressed out-of-plane expansion (reduced from +1.0% to +0.30%) of the CFO lattice near the top of nanocomposite.

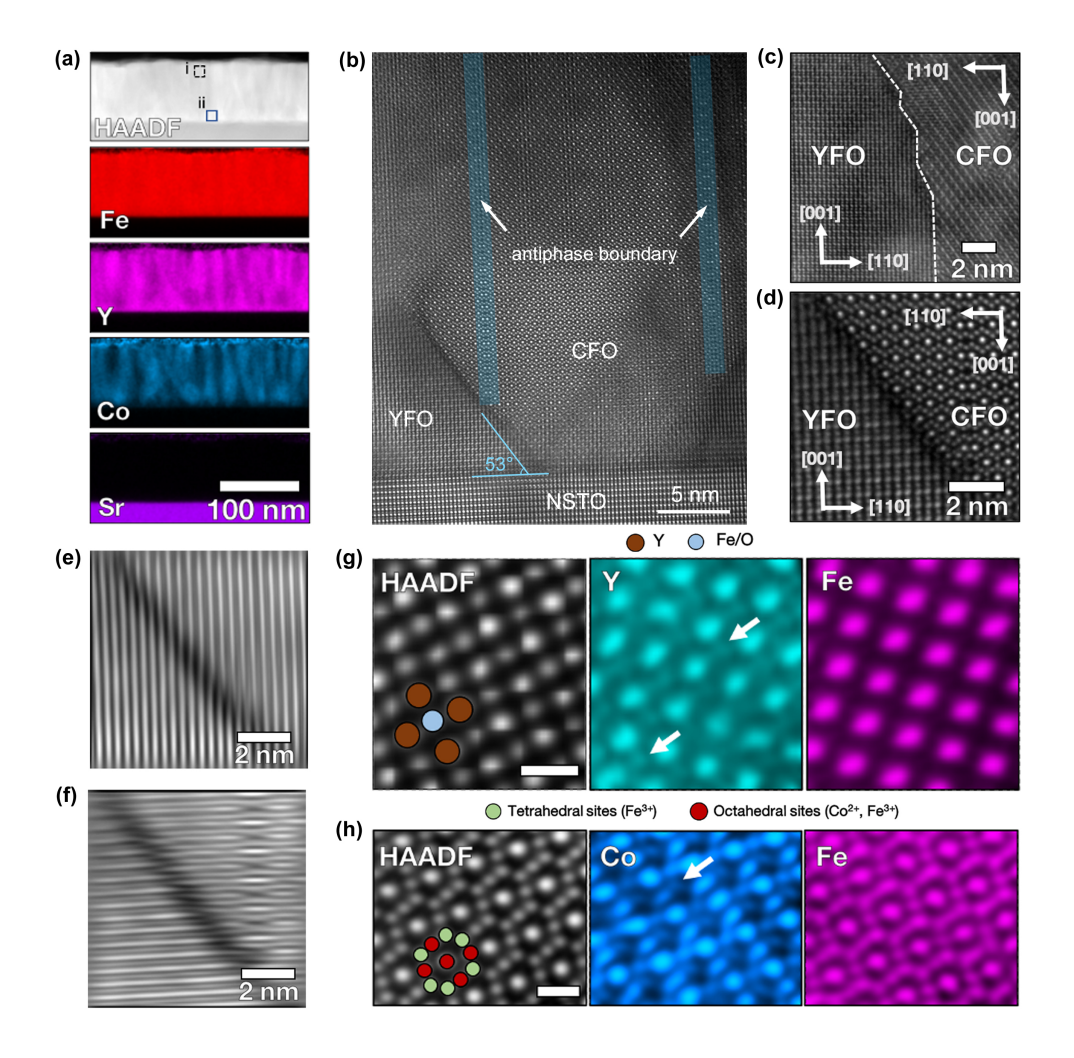


Figure 2. (a) Cross-sectional STEM imaging and EDS. (b) HAADF STEM image at CFO/YFO/STO interface viewed along [110]_{STO}. (c, d) Atomic resolution HAADF STEM of YFO-CFO interface at the (c) near the film surface and (d) at the inclined YFO/CFO interface near the substrate as marked regions i and ii, respectively, in (a). (e, f) Fourier filtered images of (d) using spatial frequencies along perpendicular directions. (g, h) HADDF STEM images and atomic resolution EDS collected at YFO (g) and CFO (h), respectively. The scale bars are 500 pm. Schematics of YFO and CFO lattice are superimposed. White arrows in (g) indicate the presence of Y_{Fe} antisite, and in (h) indicates presence of Co at tetrahedral sites.

HAADF-STEM imaging and atomic resolution EDS of the YFO and CFO are given in Figure 2g&h. Y_{Fe} antisite defects are observed in the YFO lattice indicated by the arrows in Figure 2g.

Single-phase YFO films grown under the same PLD conditions exhibit a Y:Fe ratio of 1.19, and the excess Y is accommodated as Y_{Fe} antisite defects which promote ferroelectricity via local structural distortion^[28]. The presence of Y_{Fe} in the nanocomposite suggests the same ferroelectric behavior will occur. For the CFO, atomic resolution EDS (Figure 2h) reveals that Co is present at the tetrahedral positions in addition to its occurrence on the octahedral sites typical of the inverse spinel. This indicates a partial degree of inversion, as observed in CFO prepared by other methods^[30-31]. Tetrahedral site occupancy of Co in CFO has been shown to increase the Curie temperature^[32] and magnetic moment^[33]. Additionally, anti-phase boundaries (APBs) are occasionally found in CFO as indicated in Figure 2b. Given their initiation on the inclined YFO/CFO interface, they may be the product of accommodating steps along the interface or of the nucleation and growth of different rotation variants, as previously observed in CFO thin films grown on an STO substrate^[34]. APBs are commonly observed in CFO^[35-36] and Fe₃O₄^[37], their presence may lead to reduced magnetic spin polarization^[37].

PFM was utilized to characterize the ferroelectric properties of the nanocomposite. The butterfly-shape amplitude curve (Figure 3a) and hysteresis phase loop (Figure 3b) obtained by switching spectroscopy PFM (SS-PFM) manifest repeatable ferroelectric behavior. Box-in-box writing and rewriting experiments by PFM show clear 180° PFM phase contrast in the area poled with +/-8 V (Figure 3d-f), indicating complete up/down polarization switching in the YFO component. Compared to the uniform contrast of a polarized single-phase YFO film, the small-scale features with fixed contrast and no PFM response observed in the nanocomposite originate from the CFO pillars.

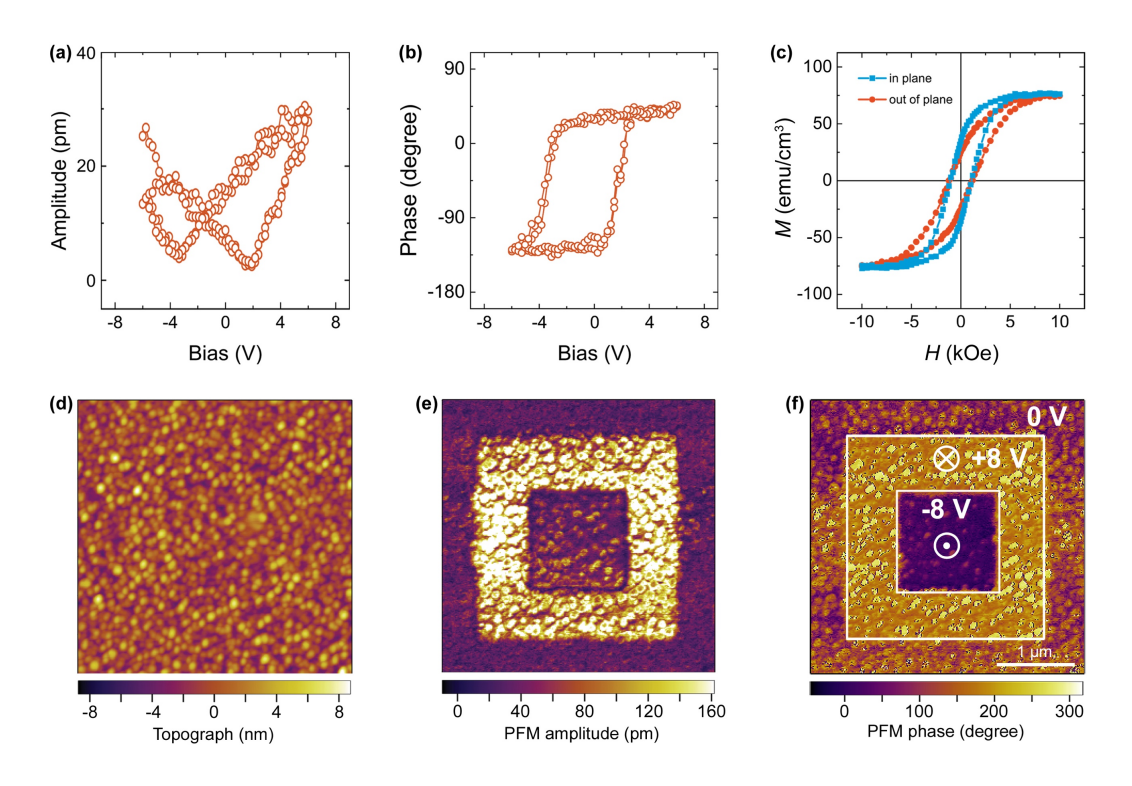


Figure 3. (a) amplitude and (b) phase curves measured by SS-PFM. (c) M-H curves measured at room temperature by VSM. (d) Topograth, (e) vertical PFM amplitude and (f) vertical PFM phase contrast images collected after the box-in-box writing process with voltages of +/-8 V as indicated in (f).

To evaluate the magnetic properties of the nanocomposite, magnetic hysteresis loops were measured at room temperature using a vibrating sample magnetometer (VSM) with the magnetic field applied both parallel (in-plane) and normal (out-of-plane) to the sample surface. The CFO is responsible for the room-temperature magnetic moment because the canted antiferromagnetic YFO perovskite saturation magnetization is about 100 times lower^[38]. The CFO volume fraction estimated from the ratio of ratio of laser shots (n_{YFO}/n_{CFO}) is about 20%. Taking this value yields a saturation magnetization (M_s) of ~375 emu cm⁻³ which is reasonably close to the M_s for bulk CFO (~400 emu cm⁻³). The lower M_s is readily explained by the approximate estimated value of

the volume fraction and/or by defects present in CFO pillars, such as deviations from stoichiometry or antiphase boundaries^[37].

The hysteresis loops indicate a remanent magnetization after saturation both in-plane and out-ofplane, but the remanence is higher and the saturation field lower when the field is applied in-plane. The aspect ratio of the pillars would favor an out-of-plane easy axis, but the in-plane compressive strain near the substrate favors an in-plane easy axis due to magnetoelastic anisotropy, considering the large negative magnetostriction coefficient $\lambda_{100} = -590 \times 10^{-6}$ of CFO^[39].

To probe the ME coupling of YFO-CFO nanocomposite, *in situ* local SS-PFM characterization was performed upon an applied magnetic field. An in-plane field of 500 Oe is too small to fully saturate the sample and produces only a small change in the SSPFM amplitude curve (Figure 4a). As the in-plane field increases to 2000 Oe, the SSPM changes in a qualitatively similar manner at different locations (Figure 4a-c). The SS-PFM amplitude curve becomes more asymmetric when the in-plane magnetic field is applied: the positive coercive voltage slightly decreases while the negative coercive voltage increases, and the amplitude for the positive electric field is larger than that for the negative electric field. Moreover, the SS-PFM phase loop shows a clear shift toward negative electric field (Figure 4d-f). Such changes collectively imply a ME coupling effect.

The ME coupling in magnetoelectric nanocomposites is believed to be mediated by strain transfer at the vertical interface between CFO and YFO. The mechanism is that a sufficiently large in-plane magnetic field reorients the magnetization of the CFO pillars in-plane, yielding an enhancement of in-plane compressive strain in the CFO pillars due to the negative magnetostriction coefficient, and hence an elongation along the out-of-plane direction. Such an out-of-plane expansion of CFO will exert an out-of-plane tensile strain on the adjacent YFO via the coherent vertical interfaces, creating an internal electric field (E_i) in the YFO due to the piezoelectric effect.

In principle, the polarity of E_i depends on the initial strain state and the strain exerted by CFO. The as-grown YFO exhibits a spontaneous polarization mostly pointing up (Figure 4g) because the non-poled region has a similar phase contrast to that of the region poled by negative DC voltages, as seen in the PFM phase contrast image (Figure 3f), and consistent with monolithic YFO thin film^[28]. Adding a tensile strain contribution yields E_i antiparallel to the initial polarization as illustrated by the schematic in Figure 4h, which accounts for the asymmetric local polarization switching curves^[40]: switching the polarization from upwards to downwards (positive DC bias) requires a smaller coercive voltage than without E_i , while switching it from downwards back to upwards requires a larger negative DC bias. The shifts towards negative DC bias direction in both amplitude curves and phase loops are also indicative of the generation of E_i upon applying the magnetic field.

We can estimate the lateral ME coupling coefficient (α_{31}) from α_{31} = $\Delta E_3/\Delta H_1$, where ΔE_3 is the change in the out-of-plane electric field, i.e., the internal electric field E_i caused by the applied inplane magnetic field ΔH_1 , that is 2000 Oe in our experiments. Given the shift of SS-PFM amplitude curves and phase loops (Figure 4a-f), the $\Delta E_3(E_i)$ can be taken as $\Delta V/D$, where D is the thickness of nanocomposite (75 nm), and ΔV is 1.0 ± 0.3 V. Therefore, α_{31} in our YFO-CFO nanocomposite is about $(6.7 \pm 2.0) \times 10^4$ mV cm⁻¹ Oe⁻¹, comparable to and even slightly larger than that of BFO-CFO self-assembled nanocomposites^[41] and PZT-CFO core–shell nanofibers^[42].

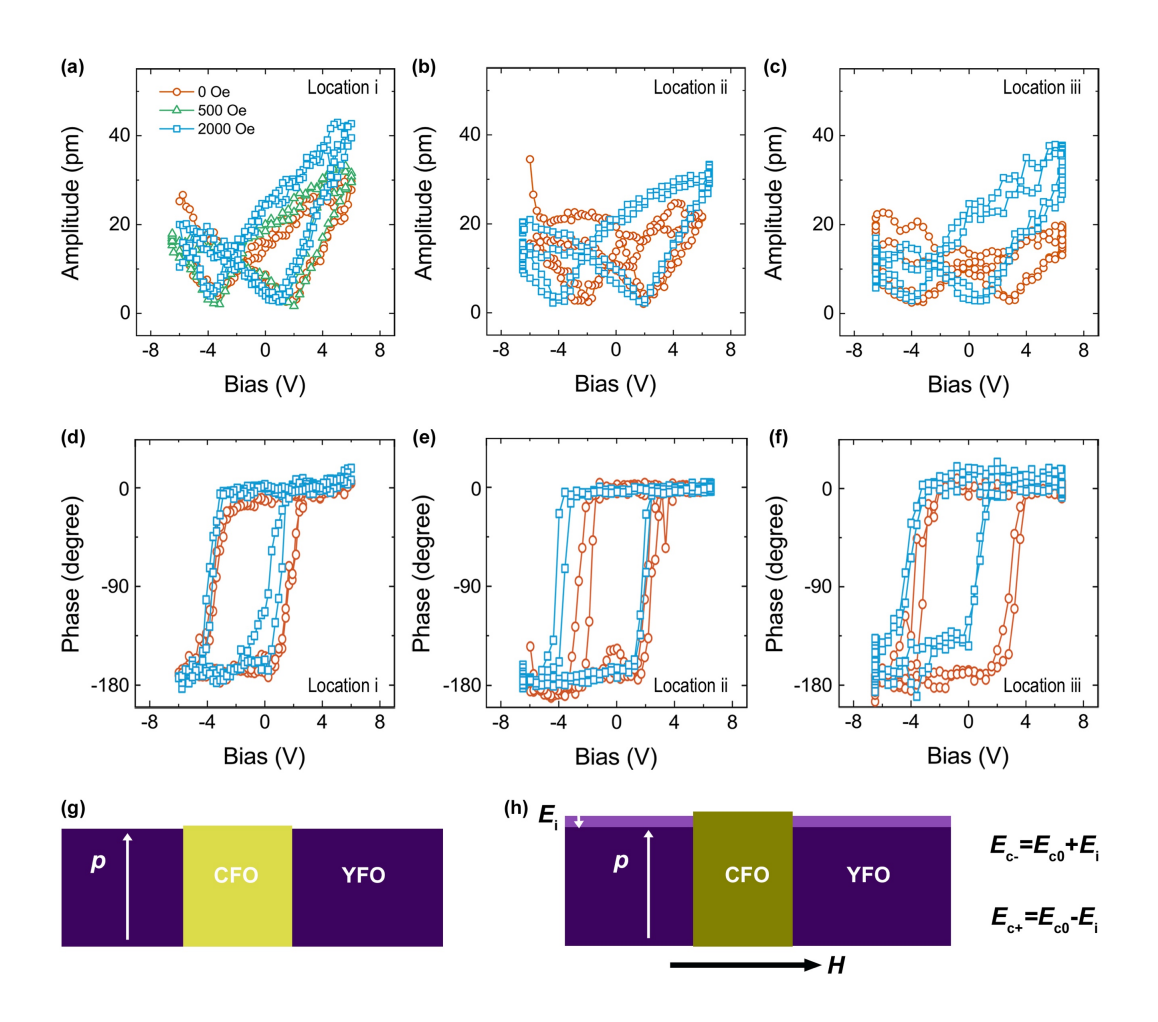


Figure 4. (a-c) SS-PFM amplitude curves and (d-f) phase loops measured at three different locations for the YFO-CFO nanocomposite thin film with and without magnetic field applied. (g, h) Schematic of the polarization in the as-grown YFO-CFO nanocomposites (g) and the strain-mediated ME coupling between CFO and YFO upon an external magnetic field.

3. Conclusion

Self-assembled, vertically-aligned nanocomposites of YFO and CFO exhibit both ferroelectricity and ferromagnetism at room temperature. The improper ferroelectric behavior originates from Y_{Fe} antisite defects in the YFO phase as reported in the single-phase Y-rich YFO films^[28], while the magnetism is primarily contributed by the CFO phase. The high density of vertical coherent interfaces between YFO and CFO enables a robust internal strain coupling and hence a noticeable

strain-mediated magnetoelectric coupling. Our results not only further corroborate the ferroelectricity in Y-rich YFO, but also demonstrate the feasibility of incorporating unconventional ferroelectrics into vertically aligned nanocomposites, providing a route to the design and synthesis of novel functional magnetoelectric heterostructures.

4. Experimental Section

Thin film preparation: The self-assembled YFO-CFO nanocomposites were prepared on NSTO substrates by pulsed laser deposition using a KrF excimer laser (λ =248 nm) with 1.3 J/cm² fluence and 10 Hz repetition rate to alternately ablate ceramic YFO and CFO targets for 200 and 50 shots respectively, so that each "layer" deposited from the targets is less than a monolayer thick. The setpoint temperature of the substrate holder was 900 °C and the substrate itself was ~100°C below this. The oxygen partial pressure, $p(O_2)$, was 10 mTorr. After growth, the films were cooled down to room temperature in the same $p(O_2)$ at a rate of 20 °C/min.

Structure characterizations: The crystalline structure was characterized by high-resolution XRD using a Rigaku SmartLab high-resolution diffractometer with Cu $K\alpha_1$ radiation (λ =1.5406 Å) as X-ray source and an incident beam Ge-(220) double-bounce monochromator. Cross-sectional samples for electron microscopy were prepared by mechanical wedge polishing with further thinning using an Ar-ion milling at cryogenic temperatures. The STEM datasets were acquired with a probe corrected Thermo Fisher Scientific Titan G3 60-300 kV operated at 200 kV. The probe convergence semi-angle was 18 mrad and the collection semi-angle range was 63–200 mrad for HAADF imaging. Atomic resolution EDS was collected with a Thermo Fisher Scientific Super-X EDS detector, and Y and Fe elemental maps were denoised using nonlocal principal component analysis using an open-source Matlab script [43] and Gaussian blurred with a standard

deviation of 1 pixel.

Magnetic and ferroelectric properties measurements: M-H curves were measured using a Digital Measurement System 7035B vibrating sample magnetometer (VSM) at room temperature. PFM measurements were performed on a commercial atomic force microscope (Cypher, Asylum Research) under single frequency and commercial dual frequency resonant tracking (DART) modes at ambient conditions with Pt-coated Si conductive probes (MikroMasch, HQ:NSC18/Pt). The magnetoelectric effect was probed by using another AFM (MFP-3D, Asylum Research) equipped with a magnetic field module.

Acknowledgements

A.K. and S.N. contributed equally to this work. This work was supported by the MRSEC Program of the National Science Foundation under award No. DMR-1419807. This work was performed in part at the Center for Nanoscale Systems (CNS), a member of the National Nanotechnology Infrastructure Network (NNIN) and part of Harvard University, supported by the National Science Foundation under award No. ECS-0335765. This work was carried in part through the use of the MIT Characterization.nano facility. A.K. and J.M.L acknowledge support from the Army Research Office under award W911-NF-19-2-0119. A.K. acknowledges support from MIT MathWorks Engineering Fellowships. S.N. acknowledges support from the National Natural Science Foundation of China (Grant No. 52102135), the State Key Laboratory of New Ceramic and Fine Processing Tsinghua University (No. KF202103), and the Fundamental Research Funds for the Central Universities (Nankai University, Grant No. 023-63213099).

References:

- [1] S. W. Cheong, M. Mostovoy, *Nat. Mater.* **2007**, *6*, 13.
- [2] N. A. Hill, *The Journal of Physical Chemistry B* **2000**, *104*, 6694.
- [3] J. V. Suchtelen, *Philips Research Reports* **1972**, *27*, 28.
- [4] C.-W. Nan, M. I. Bichurin, S. Dong, D. Viehland, G. Srinivasan, *J. Appl. Phys.* **2008**, *103*, 031101.
- [5] R. Ramesh, N. A. Spaldin, *Nat. Mater.* **2007**, *6*, 21.
- [6] Y. Wang, J. Hu, Y. Lin, C.-W. Nan, NPG Asia Materials 2010, 2, 61.
- [7] N. A. Spaldin, R. Ramesh, *Nat. Mater.* **2019**, *18*, 203.
- [8] V. Moshnyaga, B. Damaschke, O. Shapoval, A. Belenchuk, J. Faupel, O. I. Lebedev, J. Verbeeck, G. van Tendeloo, M. Mucksch, V. Tsurkan, R. Tidecks, K. Samwer, *Nat. Mater.* **2003**, *2*, 247.
- [9] H. Zheng, J. Wang, S. E. Lofland, Z. Ma, L. Mohaddes-Ardabili, T. Zhao, L. Salamanca-Riba, S. R. Shinde, S. B. Ogale, F. Bai, D. Viehland, Y. Jia, D. G. Schlom, M. Wuttig, A. Roytburd, R. Ramesh, *Science* **2004**, *303*, 661.
- [10] S. C. Liao, P. Y. Tsai, C. W. Liang, H. J. Liu, J. C. Yang, S. J. Lin, C. H. Lai, Y. H. Chu, ACS Nano 2011, 5, 4118.
- [11] R. Comes, H. Liu, M. Khokhlov, R. Kasica, J. Lu, S. A. Wolf, *Nano Lett.* **2012**, *12*, 2367.
- [12] S. Ojha, W. C. Nunes, N. M. Aimon, C. A. Ross, ACS Nano 2016, 10, 7657.
- [13] G. Tian, S. Ojha, S. Ning, X. Gao, C. A. Ross, *Adv. Electron. Mater.* **2019**, *5*, 1900012.
- [14] A. Chen, Y. Dai, A. Eshghinejad, Z. Liu, Z. Wang, J. Bowlan, E. Knall, L. Civale, J. L. MacManus-Driscoll, A. J. Taylor, R. P. Prasankumar, T. Lookman, J. Li, D. Yarotski, Q. Jia, *Adv. Sci.* **2019**, *6*, 1901000.

- [15] D. H. Kim, S. Ning, C. A. Ross, J. Mater. Chem. C 2019, 7, 9128.
- [16] X. Sun, J. L. MacManus-Driscoll, H. Wang, Annu. Rev. Mater. Res. 2020, 50.
- [17] A. Chen, Z. Bi, Q. Jia, J. L. MacManus-Driscoll, H. Wang, *Acta Mater.* **2013**, *61*, 2783.
- [18] B. B. Van Aken, T. T. Palstra, A. Filippetti, N. A. Spaldin, Nat. Mater. 2004, 3, 164.
- [19] M. Lilienblum, T. Lottermoser, S. Manz, S. M. Selbach, A. Cano, M. Fiebig, *Nat. Phys.* **2015**, *11*, 1070.
- [20] Y. K. Jeong, J. H. Lee, S. J. Ahn, S. W. Song, H. M. Jang, H. Choi, J. F. Scott, J. Am. Chem. Soc. 2012, 134, 1450.
- [21] S.-J. Ahn, J.-H. Lee, Y. K. Jeong, E.-H. Na, Y. M. Koo, H. M. Jang, *Mater. Chem. Phys.* **2013**, *138*, 929.
- [22] N. Ikeda, H. Ohsumi, K. Ohwada, K. Ishii, T. Inami, K. Kakurai, Y. Murakami, K. Yoshii, S. Mori, Y. Horibe, H. Kito, *Nature* **2005**, *436*, 1136.
- [23] D. V. Efremov, J. van den Brink, D. I. Khomskii, *Nat. Mater.* **2004**, *3*, 853.
- [24] Y. Tokura, S. Seki, N. Nagaosa, *Rep Prog Phys* **2014**, *77*, 076501.
- [25] J. H. Haeni, P. Irvin, W. Chang, R. Uecker, P. Reiche, Y. L. Li, S. Choudhury, W. Tian, M. E. Hawley, B. Craigo, A. K. Tagantsev, X. Q. Pan, S. K. Streiffer, L. Q. Chen, S. W. Kirchoefer, J. Levy, D. G. Schlom, *Nature* 2004, 430, 758.
- [26] F. Yang, Q. Zhang, Z. Yang, J. Gu, Y. Liang, W. Li, W. Wang, K. Jin, L. Gu, J. Guo, *Appl. Phys. Lett.* **2015**, *107*.
- [27] R. Gao, S. E. Reyes-Lillo, R. Xu, A. Dasgupta, Y. Dong, L. R. Dedon, J. Kim, S. Saremi, Z. Chen, C. R. Serrao, H. Zhou, J. B. Neaton, L. W. Martin, *Chem. Mater.* **2017**, *29*, 6544.
- [28] S. Ning, A. Kumar, K. Klyukin, E. Cho, J. H. Kim, T. Su, H. S. Kim, J. M. LeBeau, B. Yildiz, C. A. Ross, *Nat. Commun.* 2021, *12*, 4298.

- [29] H. Zheng, Q. Zhan, F. Zavaliche, M. Sherburne, F. Straub, M. P. Cruz, L. Q. Chen, U. Dahmen, R. Ramesh, *Nano Lett.* **2006**, *6*, 1401.
- [30] T. A. S. Ferreira, J. C. Waerenborgh, M. H. R. M. Mendonça, M. R. Nunes, F. M. Costa, *Solid State Sci.* **2003**, *5*, 383.
- [31] V. A. M. Brabers, in *Handbook of Magnetic Materials*, (Ed: K. H. J. Buschow), Elsevier, 1995, 189.
- [32] Z. Zi, Y. Sun, X. Zhu, Z. Yang, J. Dai, W. Song, J. Magn. Magn. Mater. 2009, 321, 1251.
- [33] H. Yanagihara, K. Uwabo, M. Minagawa, E. Kita, N. Hirota, *J. Appl. Phys.* **2011**, *109*, 07c122.
- [34] L. Fan, X. Gao, T. O. Farmer, D. Lee, E. J. Guo, S. Mu, K. Wang, M. R. Fitzsimmons, M. F. Chisholm, T. Z. Ward, G. Eres, H. N. Lee, *Nanomaterials (Basel)* **2020**, *10*, 472.
- [35] A. Trout, I. Pinchuk, M. Newburger, R. Kawakami, D. McComb, *Microsc. Microanal.* **2020**, *26*, 972.
- [36] G. Hu, V. G. Harris, Y. Suzuki, *IEEE Trans. Magn.* **2001**, *37*, 2347.
- [37] K. P. McKenna, F. Hofer, D. Gilks, V. K. Lazarov, C. Chen, Z. Wang, Y. Ikuhara, *Nat. Commun.* **2014**, *5*, 5740.
- [38] A. Wu, H. U. I. Shen, J. U. N. Xu, Z. Wang, L. Jiang, L. Luo, S. Yuan, S. Cao, H. Zhang, *Bull. Mater. Sci.* **2012**, *35*, 259.
- [39] R. M. Bozorth, E. F. Tilden, A. J. Williams, *Phys. Rev.* **1955**, *99*, 1788.
- [40] H. Miao, X. Zhou, S. Dong, H. Luo, F. Li, Nanoscale 2014, 6, 8515.
- [41] Z. Mo, G. Tian, W. Yang, S. Ning, C. A. Ross, X. Gao, J. Liu, *APL Materials* **2021**, *9*, 041109.
- [42] S. Xie, F. Ma, Y. Liu, J. Li, Nanoscale **2011**, *3*, 3152.

[43] J. Salmon, C. Deledalle, R. Willett, Z. Harmany, in 2012 IEEE International Conference on Acoustics, Speech and Signal Processing (ICASSP), Kyoto 2012, 1109.